Scale-up of aerated bioreactors: CFD validation and application to the enzyme production by Trichoderma reesei

Vincenzo Cappello, Cécile Plais, Christophe Vial, Frédéric Augier

Scale-up of aerated bioreactors: CFD validation and application to the enzyme production by *Trichoderma reesei*

Vincenzo Cappello[a,b], Cécile Plais[a], Christophe Vial[b], Frédéric Augier[a]

[a] *IFP Energies Nouvelles, Rond-point de l'échangeur de Solaize, BP 3, 69360 Solaize, France*
[b] *Université Clermont Auvergne, CNRS, Sigma Clermont, Institut Pascal, F-63000 Clermont-Ferrand, France*

Abstract

The application of Computational Fluid Dynamics to aerobic fermentations faces several issues, such as validation of multiphase models at high gas holdup and with complex liquids under turbulent condition. In this work, the Eulerian two-fluid model framework was adapted to simulate the enzyme production by the filamentous fungi *T. reesei*. Due to scarcity of data on turbulent mixing in complex fluids, every aspect of the numerical model (turbulence model, drag force law, rheology model, etc.) needed to be validated. First, the adequacy of the model was evaluated by the mean of comparison with new and previous experimental data in non-Newtonian aerated systems. Once coupled with an apparent oxygen and substrate uptake kinetics, the model was used to investigate the effect of scale-up on the enzyme productivity from biomass. Fully predictive results highlighted complex behaviors, such as: possible substrate heterogeneities, yield loss, and non-obvious interactions between mixing and oxygen transfer limitations.

Keywords: Two-phase model, CFD, non-Newtonian, Multiphase bioreactor, Biomass, Scale-up

1. Introduction

Industrialization of biological cultures faces many challenges. In particular, the reactor scale-up generates important modifications on the microorganism environment. At larger scales, good mixing can be difficult to achieve, because of the high circulation time that can lead to the formation of substrate heterogeneities including carbon sources, but also dissolved oxygen in aerobic fermentations (Haringa et al., 2016; Doran, 2013; Enfors et al., 2001). The main characteristics of these heterogeneities — magnitude, spatial distribution — depend on many factors, such as cell metabolism and substrate uptake on the one hand, and transport phenomena on the other, including fluid dynamics and nutrients dispersion. Consequently, to correctly scale-up a bioreactor two questions related to substrate and oxygen heterogeneities can be addressed:

- What kind of heterogeneities would be generated under the considered conditions (reactor geometry, operating conditions)?
- How heterogeneities would impact the fermentation yield?

The first question challenges the ability to predict spatial distributions of substrate concentrations during scale-up calculations, and it is the main topic of the present study. The second question is directly addressed by scale-down experimental methods, which aim to study the fermentation yield in some simple but relevant situations, as a bi-zone bioreactor or a single reactor with temporal steps of substrate injection (Paul et al., 2004; Oosterhuis et al., 1985).

Among the variety of biological productions that are concerned by scale-up and scale-down optimization, the case of filamentous fungi is here considered. Particularly, due to its natural high secretion capacity, *Trichoderma reesei* is used to produce enzymes for lignocellulosic ethanol processes (Li et al., 2016; Gusakov, 2011). The scale-up of related bioreactors is complex due to the combination of high Oxygen Uptake Rate (OUR), the non-Newtonian rheology of the broth and its negative effect on the oxygen mass transfer (Petříček et al., 2018; Bach et al., 2017; Gabelle et al., 2012). Moreover, to maximize the protein yield and cope with the growing biofuel market, very large fermenters are needed.

In industry, scale-up is classically based on the prediction of macroscopic variables, assuming spatial homogeneity of all concentrations and transport phenomena. This approach is based on empirical models to predict apparent rheology, mass transfer and, finally, the fermentation yields. The presence of heterogeneities can only be suspected from the calculation of mixing time and its comparison with the biological timescales. Alternatively, Computational Fluid Dynamics (CFD) is more and more used to predict the flow field and spatial distributions of reactants in various reactors and bioreactors (Haringa et al., 2018; Gradov et al., 2017; Morchain et al., 2014). Concerning the investigation of aerobic fermentations, the use of CFD is not outstretched yet due to the lack of physical models and appropriate validation; particularly for *T. reesei* cultures, the complex rheology makes the use of CFD even more questionable. Because of the lack of experimental data at high gas holdup (even in Newtonian liquids), very few CFD studies have dealt with such complex systems (Haringa et al., 2018; Bach et al., 2017).

A two-fluid Eulerian CFD framework — the only one actually usable at industrial scale and high gas flow rates — was proposed in the present study, in agreement with similar studies. In the

second part of the results section, the validation and capability of this approach to simulate hydrodynamics, mixing and mass transfer in non-Newtonian aerated fluids was discussed. An extensive previous experimental work allowed us to characterize bubble sizes, gas-holdup, mixing and mass transfer under different stirring conditions (Cappello et al., 2020). This experimental background served both to develop an appropriate mass transfer model and to obtain a large database used to validate the numerical models. Despite some spatial differences on gas dispersion, and residual discrepancies on global variables, such as mixing time, power input, overall gas holdup, and mass transfer, the global behavior of the model appeared as rather faithful and usable to investigate the effect of scale-up on cultures. Finally, the model was coupled with oxygen mass transfer, and with a simple metabolic model to describe the enzyme production by *T. reesei*. The application of the model to different geometries and sizes of bioreactors illustrates the interest of the approach and its capability to predict substrate heterogeneities and associated loss of fermentation yield.

2. Methods and materials

2.1. Experimental methods and database

Numerical results were validated with experiments carried out at two reactor scales, whose main geometrical details are listed in table 1. Moreover, three geometries for the CFD simulation of *T. reesei* fermentation were considered, going from $0.02\,\mathrm{m}^3$ to $100\,\mathrm{m}^3$, as described in section 2.4; a $22\,\mathrm{m}^3$ four-impeller configuration was also simulated.

To analyze the influence of viscosity, xanthan gum was dissolved in tap water, and two concentration of the polymer (0.25 and 0.50%) were considered. As reported by Gabelle et al. (2012), xanthan gum solutions and *T. reesei* present a comparable rheological behavior. In figure 1 the apparent viscosity of *T. reesei* at different cell concentration (C_X) is compared to the xanthan gum viscosity.

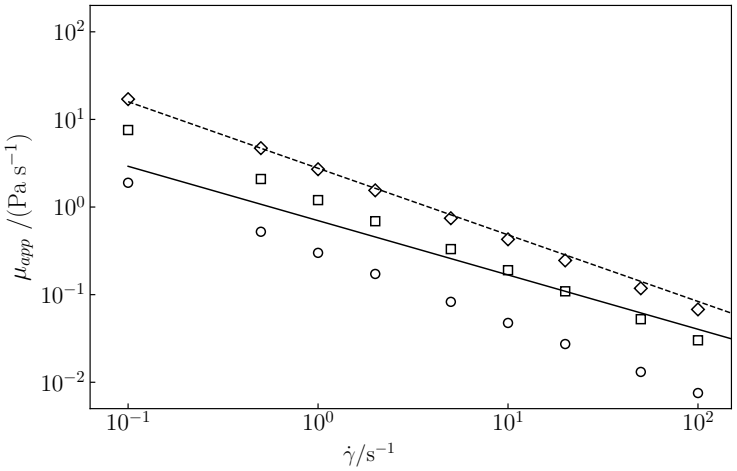

Figure 1: Rheology of fermentative broth at diffent biomass concentrations and during the production phase. Data: $C_X = 10\,\mathrm{g\,L^{-1}}$ (○), $C_X = 20\,\mathrm{g\,L^{-1}}$ (□), $C_X = 30\,\mathrm{g\,L^{-1}}$ (◇), xanthan gum 0.25% (——), and xanthan gum 0.50% (----).

The mixing time was measured in the small tank T_{30}, in water and xanthan gum solutions. Mixing time was calculated by using a colorimetry technique: $10\,\mathrm{ml}$ of a dye (Drimaren violet

Table 1: Characteristic dimensions of the tanks. For the explanation of the symbols, refer to figure 3

Size in m	T_{30}	T_{60}
T	0.3	0.6
D	0.1	0.2
H	0.3	0.6
h_D	0.1	0.2
h_S	0.05	0.1
B	0.02	0.04

R-2RL) was injected in the liquid, and its variation over time was recorded with a camera Nikon D300S (Gabelle, 2012).

A modified Pitot tube (or Pavlov tube) was used to measure the radial liquid velocity inside the tank T_{60}. Velocity measurement was done by measuring the differential pressure between two perpendicular tubes. Thus, according to Bernoulli's equation, the mean local velocity can be obtained by averaging the instantaneous velocities:

$$V_l = \frac{\sum_{i=1}^{N} u_i}{N} \text{ with } u_i = \begin{cases} \left(\frac{2\Delta P_i}{\rho_l}\right)^{0.5} & \text{if } \Delta P_i \geq 0 \\ -\left(\frac{-2\Delta P_i}{\rho_l}\right)^{0.5} & \text{if } \Delta P_i < 0 \end{cases} \tag{1}$$

where u_i is the instantaneous velocity calculated from the kinetic energy balance, ΔP_i is the differential pressure captured at the instant i and $N$is the total number of acquisitions. More information on the Pavlov tube and its use in bubbly flows can be found in Forret et al. (2003). The Pavlov tube that was used in this study was made of four stainless L-shape $5\,\mathrm{mm}$ diameter tubes that were arranged inside a stainless supporting tube with a diameter of $40\,\mathrm{mm}$. Figure 2 shows the measuring probe of the Pavlov tube. The equipment was introduced from the top of

Figure 2: Detail of the measuring tip of the Pavlov tube.

the vessel with the aid of a moving support. The differential pressure was measured by means of a pressure transmitter of the PD-33 X series (Keller, Winterthur, Switzerland) and the acquisition time was two minutes at a frequency of $400\,\mathrm{Hz}$.

Results in terms of bubble size, gas holdup, and volumetric mass transfer coefficient were obtained from Cappello et al. (2020), who reported experimental data collected for the same tank sizes simulated in this study. In table 2, the list of the measured quantities and the relative operating conditions are shown.

Table 2: Experimental quantities with respective range of operating conditions used for CFD validation.

Quantity	Tank	System	P_g/V $\mathrm{W\,m^{-3}}$	U_g $\mathrm{mm\,s^{-1}}$	Reference
Mixing time	T_{30}	W, XG	200–6000	0–40	This study
Radial liquid velocity	T_{60}	W	500–4000	0–4	This study
Gas holdup	T_{30}, T_{60}	W, XG	700–6000	4–40	Cappello et al. (2020)
Sauter mean diameter	T_{30}, T_{60}	W, XG	700–6000	4–40	Cappello et al. (2020)
k_La	T_{30}, T_{60}	W, XG	700–6000	4–40	Cappello et al. (2020)
RPD	T_{30}, T_{60}	W, XG	200–6000	0–40	Gabelle et al. (2011)

2.2. Numerical settings

All the simulations were carried out in ANSYS Fluent 2019 R2 (v.19.4). Equations for momentum and continuity were solved by using the pressure-based coupled algorithm; compared to the segregated algorithm, the coupled one gave more stable simulations with the same accuracy, especially in the case of multiphase simulations. The coupled solver requires more memory, because momentum and pressure-based equations are solved simultaneously at the same step. Nevertheless, CFD robustness benefits from it and less iterations are usually necessary to achieve convergence (Keating, 2011).

Second-order schemes were used for the discretization of velocity, pressure, and turbulent quantities equations, whereas the volume fraction equation was discretized with a first-order scheme — more stable than the second order, which led to divergence of the simulations. The underestimation of turbulent kinetic energy and its dissipation rate in agitated tanks simulations is a known issue (Lane, 2017; Singh et al., 2011). To solve this problem, the use of high-order schemes for convection terms has been advised by different authors (Deglon and Meyer, 2006; Aubin et al., 2004). Together with the discretization scheme, the mesh resolution greatly affects the computation of turbulent quantities; in order to have a good estimation of the hydrodynamics, at least ten nodes are needed along the impeller blade height (Gimbun et al., 2009).

The rheology of the complex liquid was described with the power-law model:

$$\mu_{app} = K\dot{\gamma}^{n-1} \tag{2}$$

where K and n are the consistency and flow indexes, respectively. The correlation proposed by Pérez et al. (2006) was used to compute the local shear rate $\dot{\gamma}$; based on their model, the shear rate can be expressed in terms of turbulent energy dissipation rate, ε:

$$\dot{\gamma} = \left(\frac{\rho_l \varepsilon}{K}\right)^{\frac{1}{1+n}} \tag{3}$$

Turbulence was modeled with the realizable k-ε model, and its *dispersed* formulation was used for multiphase cases. Equations for turbulent quantities were then solved only for the liquid phase and used to derive the ones for the gas phase.

The multiphase Eulerian model was used, and only the drag force was considered in the description of the interphase forces; additional forces such as lift and turbulent dispersion forces

were considered as well, but the use of these terms did not lead to a clear improvement of the results. In air-water simulations, the universal drag laws provided the better results, while the drag coefficient (C_D) proposed by Scargiali et al. (2007) was adopted in the case of aerated complex liquids:

$$C_D = \frac{4}{3}\frac{d_{32}}{U_t^2}\frac{g\,(\rho_l - \rho_g)}{\rho_l} \tag{4}$$

where U_t is the bubble terminal velocity, d_{32} is the Sauter mean bubble diameter, and ρ_l and ρ_g are the liquid and gas densities, respectively. The bubble terminal terminal velocity was estimated via the correlation of Mendelson (1967):

$$U_t = \left(\frac{2.14\,\sigma}{\rho_l\,d_{32}} + 0.505\,g\,d_{32}\right)^{0.5} \tag{5}$$

Here, σ is the surface tension, that was set to $0.072\,\mathrm{N\,m^{-1}}$.

Moreover, the Multiple Reference Frame (MRF) approach was employed to describe the impeller rotation after comparison with the sliding mesh (SM) method. In the SM approach, the mesh is subdivided into a moving part close to the impeller that follows the rotation of the paddles on the one hand, and a static part with respect to the tank on the other hand, separated by a sliding interface. This implies transient simulations, and information about momentum and pressure are exchanged through the interface between these two zones. Unlike the SM method, in the MRF approach the moving part is frozen and solved in a rotating reference frame accounting for centrifugal and Coriolis forces in the momentum equations while the equations of the static region remain unchanged. A steady state solution can thus be obtained. For estimation of global hydrodynamics in standard tank configurations, the MRF model has been found computationally more efficient (Aubin et al., 2004; Shi and Rzehak, 2018). Cases were solved with steady state formulation, and the pseudo-transient method was used to further improve stability. The pseudo-transient formulation introduces implicit under-relaxation factors, that are based on a pseudo-time step (ANSYS Fluent Theory Guide, 2019).

Finally, the simulation was considered converged when the torque on the shaft, liquid average velocity, turbulent dissipation rate, and average gas fraction were constant within $\pm 3\%$ of their final values.

2.2.1. Computational grid and boundary conditions

The validation study was done by comparing numerical values with experimental data obtained in two agitated vessels of different sizes, T_{30} and T_{60} (Cappello et al., 2020), already described in section 2.1. For both tank sizes, the mesh was created via meshing tools included in the ANSYS suite. Thanks to the symmetry of the system, a completely hexahedral mesh could be designed (figure 3). A preliminary mesh sensitivity study — in which four different mesh resolutions up to $5 \cdot 10^6$ cells were considered — showed that a mesh with twenty cells along the blade height can provide accurate results, in terms of both local and global quantities; for the configuration T_{60}, a mesh with $6 \cdot 10^5$ elements was used for the validation study. A further increase in the number of cells led only to a negligible improvement (less than 1%) of the power estimation.

Moreover, by treating the lateral surfaces as periodic boundaries, only a sixth of the tank was modeled; this simplification has been already used in several studies, where only half or a sixth

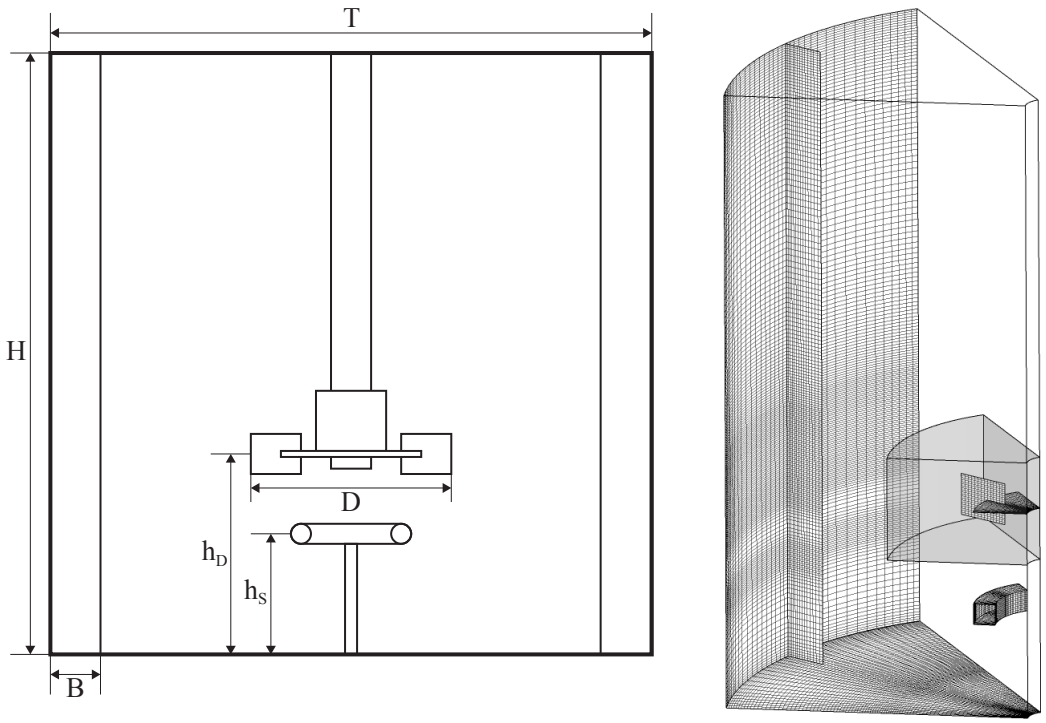

Figure 3: Geometrical details of the reactor and its mesh. Refinement of the mesh in the rotating zone and along the sparger walls can be noticed; the MRF volume is also highlighted.

of the actual geometry were simulated (Haringa et al., 2018; Lane et al., 2005; Liangchao et al., 2018). Simulations on a full geometry were run to check the influence of the periodicity condition, confirming that this approach led to good estimation of the global liquid and gas characteristics, as shown at the beginning of the results section.

The top free surface was defined with a degassing boundary condition, that acts as a free-slip wall for the liquid phase and an outlet for the dispersed phase, which leaves the domain.

Except for the impeller and the shaft, all the other walls were defined as no-slip walls for the continuous phase and as free-slip walls for the dispersed one. To take into account the accumulation of gas in the impeller region, impeller and shaft were modeled with a no-slip conditions for both phases instead. The scalable wall function was adopted to deal with turbulence in the regions close to walls.

Gas injection was modeled with a velocity inlet boundary condition at the top surface of the sparger. To avoid unnecessary complications, the injection surface was meshed as a flat surface, rather than considering the real pierced rounded sparger. The inlet volume fraction of the dispersed phase was set to unity.

2.3. Metabolic kinetics

Proteins production was described via a Monod-type kinetic model. Other similar models are available in the literature (Lo et al., 2010). Rate of cell (X) growth, rates of substrate (S), oxygen

Table 3: Kinetic constants used in Eqs. (6)–(13).

Parameter	Value	Description
μ_{max} / $(\mathrm{h}^{-1})^{\dagger}$	0.05–0.15	Maximum growth rate
K_{μ_S} / $(\mathrm{g_S\,L^{-1}})^{n_\mu}$	1	Substrate affinity to biomass
K_{μ_O} / $(\mathrm{g_O\,L^{-1}})$	0.002	Oxygen affinity to biomass
$q_{P_{max}}$ / $(\mathrm{g_P\,g_X^{-1}\,h^{-1}})^{\dagger}$	0.015–0.030	Maximum production rate
$q_{P_{min}}$ / $(\mathrm{g_P\,g_X^{-1}\,h^{-1}})$	0.002	Minimum production rate
$K_{in.}$ / $(\mathrm{g_S\,L^{-1}})$	1	Growth/production threshold
K_{P_S} / $(\mathrm{g_S\,L^{-1}})$	0.001	Substrate affinity to substrate
K_{P_O} / $(\mathrm{g_O\,L^{-1}})$	0.002	Oxygen affinity to substrate
n_μ	3	
$n_{in.}$	3	
$Y_{X,O}$ / $(\mathrm{g_X\,g_O^{-1}})$	0.98	Conversion-to-biomass yield
$Y_{P,O}$ / $(\mathrm{g_P\,g_O^{-1}})$	1.03	Conversion-to-substrate yield
$Y_{X,S}$ / $(\mathrm{g_X\,g_S^{-1}})$	0.5	Conversion-to-biomass yield
$Y_{P,S}$ / $(\mathrm{g_P\,g_S^{-1}})$	0.5	Conversion-to-substrate yield

† For confidentiality reasons, only a range is provided.

(O_2) consumption, and rate of products (P) formation can be expressed by the following equations:

$$\frac{dC_X}{dt} = \mu_X C_X \tag{6}$$

$$\frac{dC_P}{dt} = q_P C_X \tag{7}$$

$$\frac{dC_S}{dt} = -q_S C_X + q_{feed} \tag{8}$$

$$\frac{dC_{O_2}}{dt} = -q_O C_X + k_L a \left(C^*_{O_2} - C_{O_2}\right) \tag{9}$$

Here, $C^*_{O_2}$ is the oxygen solubility, whereas q_P and μ_X represent the specific protein production rate and the specific growth rate, respectively. These kinetic variables are defined as:

$$\mu_X = \mu_{max} \frac{C_S^{n_\mu}}{K_{\mu_S} + C_S^{n_\mu}} \frac{C_{O_2}}{K_{\mu_O} + C_{O_2}} \tag{10}$$

$$q_P = \left[\frac{q_{P_{max}} - q_{P_{min}}}{1 + \left(\frac{C_S}{K_{in.}}\right)^{n_{in.}}} + q_{P_{min}} \right] \frac{C_S}{K_{P_S} + C_S} \frac{C_{O_2}}{K_{P_O} + C_{O_2}} \tag{11}$$

The values and the definition of each parameter are reported in table 3.

Figure 4 shows $q_P/q_{P_{max}}$ and μ_X/μ_{max} without oxygen limitations (i.e. $C_{O_2} = 0.008\,\mathrm{g\,L^{-1}}$). Two regimes can be identified depending on the substrate concentration. At $C_S < 0.1\,\mathrm{g\,L^{-1}}$, the substrate concentration is too low to favor the cell growth; in this environment, the biomass mainly

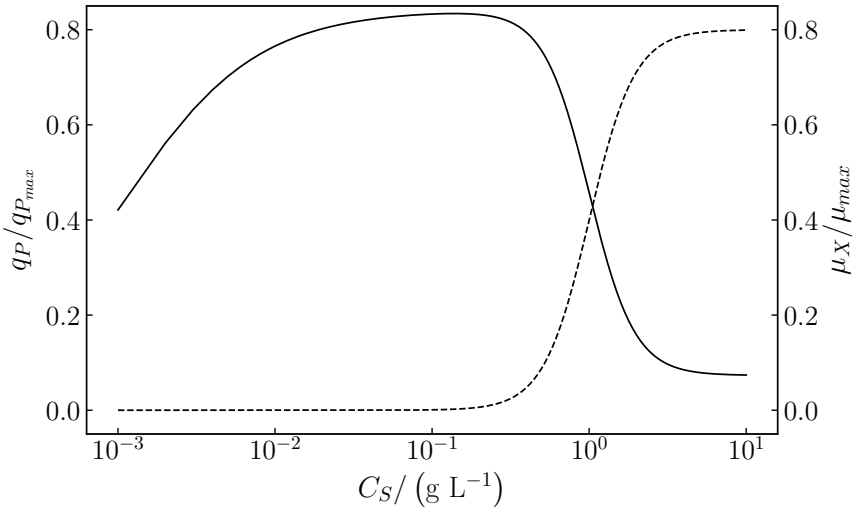

Figure 4: Influence of the substrate concentration on the specific production rate q_P (—) and specific growth rate μ_X (----) at $C_{O_2} = 0.008\,\mathrm{g\,L^{-1}}$.

secretes proteins. The production rate is maximum in the concentration range $\sim$0.01–0.1 $\mathrm{g\,L^{-1}}$. Increasing nutrient concentrations has a negative effect on the protein yield; at C_S greater than $1\,\mathrm{g\,L^{-1}}$, the substrate is mainly consumed by the microorganisms to grow. Finally, the oxygen uptake q_O and the substrate consumption rate q_S are defined as follows:

$$q_O = \frac{\mu_X}{Y_{X,O}} + \frac{q_P}{Y_{P,O}} \tag{12}$$

$$q_S = \frac{\mu_X}{Y_{X,S}} + \frac{q_P}{Y_{P,S}} \tag{13}$$

where $Y_{X,O}$, $Y_{P,O}$, $Y_{X,S}$, and $Y_{P,S}$ are yield coefficients (table 3).

The CFD model described an instantaneous condition of the real fed-batch fermentation, at the beginning of the production phase. Therefore, a constant concentration of biomass C_X was considered, and only Eqs. (8) and (9) were solved in steady state. After reaching a converged gas-liquid mixing simulation, equations of momentum, turbulence, and volume fraction were deactivated, while the species equations for the nutrients were activated. Transport equations for the substrate and oxygen concentrations were discretized using a second-order upwind scheme. The substrate feed (q_{feed}) was modeled by defining a source term in a small area close to the top surface; results were then analyzed at two feed rates, q^I_{feed} =0.015–0.020 $\mathrm{g_S\,g_X^{-1}\,h^{-1}}$ and $q^{II}_{feed} = 2q^I_{feed}$. Here again, only a range of values could be provided for confidentiality of the *T. reesei* strain characteristics.

2.4. Overview of the cases

2.4.1. Validation of CFD models

Numerical results for T_{30} and T_{60} were validated against experimental data previously obtained (Cappello et al., 2020) and predicted values from empirical correlations (Gabelle et al., 2011; Cappello et al., 2020). The measured Sauter mean diameter was used as a parameter in the simulations,

while the global gas holdup, the mixing time, and the Relative Power Demand (RPD) served to assess the accuracy of the simulation. The correlation proposed by Gabelle et al. (2012) was used to predict the RPD:

$$\text{RPD} \equiv \frac{P_g}{P_0} = \max\left[0.33; exp\left(-15.36 N_P^{0.16} Q_g^{0.62} T^{-1.7}\left(\frac{D}{T}\right)^{0.51}\right)\right] \tag{14}$$

where P_g is the power draw, P_0 the power consumption in non-aerated condition, Q_g the gas flow rate, and N_P the impeller power number.

The validity of the CFD models was studied for the following range of superficial gas velocities: U_g =1–40 mm s^{-1}. At these conditions, the average bubble size varied between 3.4–6 mm, with the higher values in the case of complex liquid phase (Cappello et al., 2020). Several impeller rotation speeds were also considered, so that the dissipated power was in the range of 700–4000 W m^{-3}.

2.4.2. Application to Trichoderma reesei fermentation

The main goal of the numerical study was to address the problem of designing large-scale fermenters. In that configuration, the role of substrate gradients in the productivity of the system has to be considered. In order to generate these gradients, bigger tanks were simulated, as the mixing time scales with the impeller speed. Therefore, besides the tank T_{30} that was used for the validation of the closure models, two other tanks were simulated; these had a volume of about 100 and 20 m^3. In table 4, the details of each configuration are reported. The case 4R refers to a four-impeller configuration, which was used to extend the CFD model to a more practical problem. At industrial scale, in fact, when high volumes of liquid are processed, units with $H : T > 1$ are usually more convenient. In figure 5, the diagram of the multi-stage reactor is shown.

By comparing the characteristic times of the process, one can predict the formation of spatial gradients. In particular, one can define a Damköhler number, Da as:

$$Da = \frac{\theta_c}{\theta_S} \tag{15}$$

Here, θ_c is the characteristic flow time, usually taken as the circulation time ($\theta_c \approx \theta_{95}/4$ in stirred tanks), whereas θ_S is the reaction time. In this study, the substrate was the limiting reactant; therefore, the reaction time scale was defined in terms of average substrate consumption:

$$\theta_S = \frac{\langle C_S \rangle}{C_X \, q_S} \tag{16}$$

Table 4: Tank configurations used with the fermentation model.

Case	T m	$H : T$	V_l m^3
1S	0.3	1	$2 \cdot 10^{-2}$
1B	5.0	1	98
4R	2.1	3	22

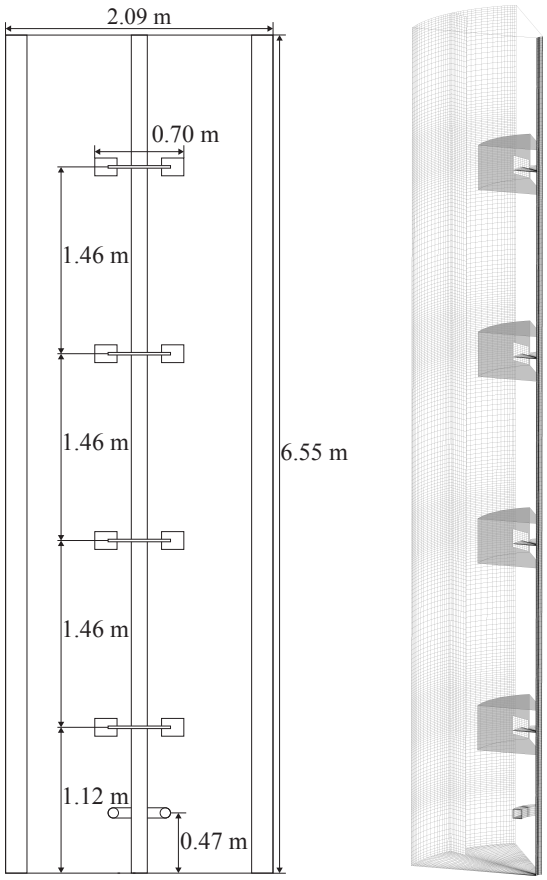

Figure 5: Scheme of the $22\,\mathrm{m}^3$ reactor with four Rushton turbines. On the right, details on the mesh used to model a sixth section of the tank.

When Da is greater than one, the reaction timescale is lower than the circulation one. In this scenario, the substrate gets consumed quickly before getting uniformly mixed inside the reactor, leading to the formation of concentration gradients. Finally, the characteristic mass transfer timescale $(1/k_La)$ was considered as well. In table 5, the operating conditions and different timescales are listed for the three configurations described above. For all the three simulation cases, the rotation

Table 5: Operating conditions and timescales in for mixing, mass transfer, and substrate consumption in different configurations at $C_X = 20\,\mathrm{g\,L^{-1}}$. For confidentiality reasons, only the feed rates $q_{feed}/(\mathrm{g_S\,g_X^{-1}\,h^{-1}})$ were reported in terms of interval.

Configuration	N / $\mathrm{s^{-1}}$	q_g / vvm	θ_c / s	$(k_La)^{-1}$ / s	q^I_{feed} =0.015–0.020 θ_S / s	$q^{II}_{feed} = 2q^I_{feed}$ θ_S / s
1S	13.3	1.7	1	40	10	1950
1B	1.6	0.1	5	63	10	1950
4R	2.7	$7.6 \cdot 10^{-2}$	27	60	10	1950

speed and gas flow rate were chosen in order to have $P_g/V_l = 2300\,\mathrm{W\,m^{-3}}$ and a superficial gas velocity of $8.3\,\mathrm{mm\,s^{-1}}$, which correspond to common operating conditions for an industrial fermentation; the same average bubble diameter equal to $4.1\,\mathrm{mm}$ — experimentally measured for the configuration 1S — was adopted for the 1B and 4R cases. The mass transfer mechanism at the fermentation conditions was computed with the following equations (Cappello et al., 2020):

$$k_L/(\mathrm{m\,s^{-1}}) = 9.2 \cdot 10^{-5}\ \mu_{app}^{-0.26} \tag{17}$$

The predicted performance of each configuration was evaluated in terms of normalized protein production rate, q_P^*, and normalized growth rate, μ^*:

$$q_P^* = \frac{q_P}{q_{P_{max}}} \tag{18}$$

$$\mu^* = \frac{\mu}{\mu_{max}} \tag{19}$$

3. Results and discussion

3.1. Validation of closure models

3.1.1. Accuracy of MRF approach and partial domain

In figure 6, the gas fraction at the impeller plane for both MRF and SM models is shown. At the considered operating conditions, the tank was characterized by $Fl_g = 0.04$ and $Fr = 1.81$; for this set of values, the $3-3$ cavity structure was expected. Obviously, due to the periodic boundary conditions, such a structure could not be obtained with a partial domain (figure 6a). However, the simulation of the entire geometry figure 6b was capable of reproducing the alternating pattern of the gas cavities, with three clinging cavities and three large cavities. Interestingly, in the case of the partial geometry, it seemed that the size and shape of aerated cavities were in between the ones of the full geometry. From table 6, it can be seen that even with a partial periodic geometry, the global quantities were predicted with acceptable accuracy.

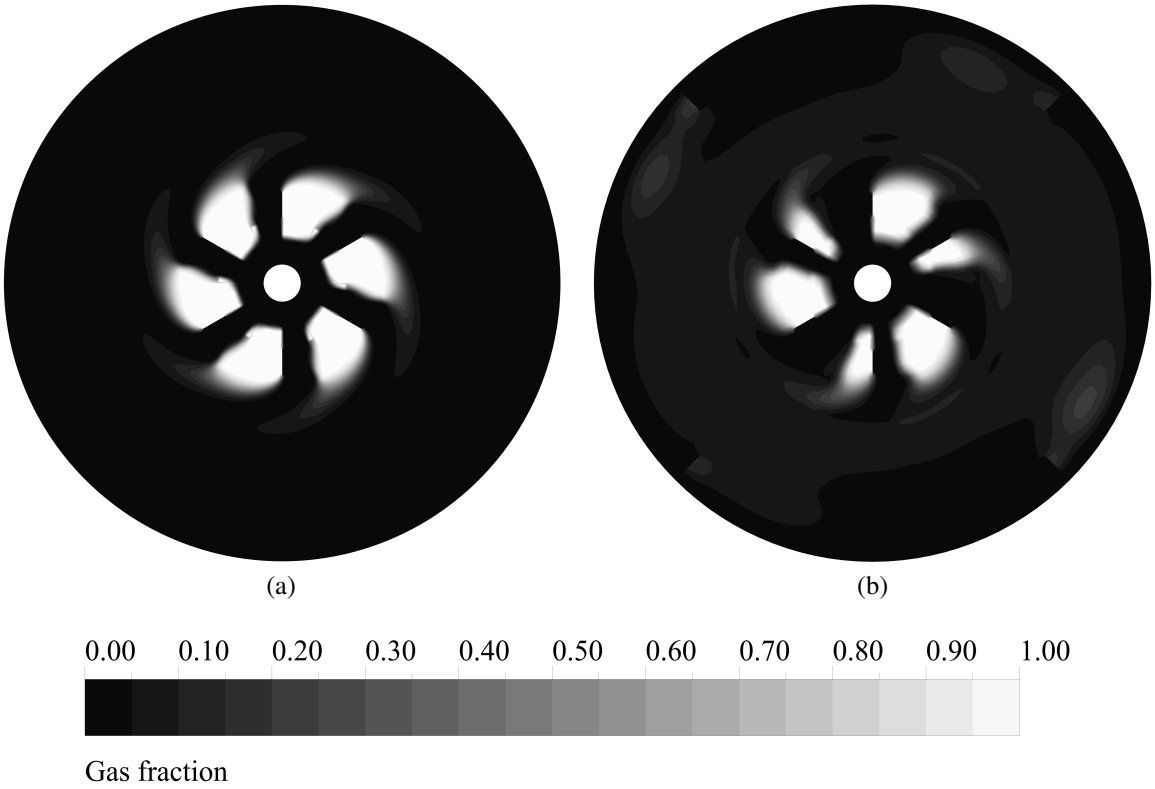

Figure 6: Gas cavity structures at $U_g = 8\,\mathrm{mm\,s^{-1}}$ by using MRF (a) and SM models (b). A sixth of the domain was simulated in the case of the MRF approach; to facilitate the comparison, the partial geometry was repeated in post-processing to represent the full tank.

Additionally, the rotation model did not have a strong impact on the global hydrodynamics, as it can be seen in table 6. Comparable errors were in fact obtained with both models. The Relative Power Demand was better predicted with the full geometry and sliding mesh model, probably because of the more accurate representation of the aerated cavities. Nevertheless, in the

perspective of industrial scale simulations, the simpler MRF approach with the periodic geometry was retained, as it was the best compromise between the results accuracy and the CPU time. In fact, by using the steady MRF model and the periodic domain, convergence was achieved five times faster. A full geometry is however recommended when gas structures behind the impellers need to be accurately predicted, for example to study transitions between the different aerated regimes.

3.1.2. Air-water simulations

Local gas fraction profiles are shown in figure 7. The numerical model performed well in describing the gas fraction at the impeller discharge region (figure 7c). However, simulations were less accurate to reproduce the sampled gas fractions at higher axial locations. In fact, the gas fraction close to the walls was underpredicted. In contrast to experimental findings, predicted profiles of the gas volume fraction decayed very fast when moving towards the vessel walls. Therefore, numerical data were characterized by a mean error of 38%. These findings seem to suggest that simulations at this gas flow rate might underestimate the gas dispersion in the tank.

In figure 8, the gas distribution computed with the universal drag laws at two tank sizes is compared with experimental results of Bombač et al. (1997). The comparison is intended to be only qualitative, because of the different operating conditions considered by Bombač et al. (1997). However, in all cases impeller speed and gas flow rate were such that hydrodynamics was characterized by the vortex-clinging (VC) cavity structure, so a similar gas distribution was expected. As shown in the figure, the accumulation of the gas in the recirculation loops was reproduced, even though the amount of gas inside the loops was probably overestimated in the small tank.

The presence of these gas pockets could not be solved even by implementing other interphase forces, such as lift and turbulent dispersion forces. While the latter term did actually help to have a more homogeneous gas distribution, it also disrupted the gas cavities behind the impeller, with a negative effect on the dissipated power, leading to an erroneous estimation of the impeller power number. This is certainly the major identified weakness of the developed model, which will require further improvements. However, from figure 8b it appears that a better gas distribution was computed for the geometry 1B. At this scale, the turbulent viscosity could be high enough to mask the contribution of other forces to disperse gas bubbles; in fact, for the same dissipated power, the Reynolds number for the reactor 1B was more than thirty times higher than the one for 1S, while the turbulent viscosity ratio was even greater.

Table 6: Effect of geometry and rotation model on global holdup and RPD.

Case	RPD	Gas holdup
Partial, MRF	0.49	0.068
Full, SM	0.45	0.075
Experimental	0.41*	0.072

*Extracted from Gabelle (2012).

Global holdup and gassed power consumption. In figure 9a, the global gas fraction for both tanks T_{30} and T_{60} is presented. Numerical data were compared with holdup measurements described in Cappello et al. (2020). Gradual increase in gas holdup with the injection rate is expected, and simulated cases showed this trend. From the graph, it can be seen that numerical data for both tanks diameters were practically the same, as in the case of experimental findings. Errors on numerical values were about 10%, that is in the same order of magnitude of the measurement precision.

Formation of gas cavities behind the impeller's blades causes modification on the energy supplied to the liquid, and has an impact on the reactor hydrodynamics. In fact, the decrease in power input in gas-liquid reactors depends on the shape and pattern of these cavities (Paul et al., 2004). In figure 9b, RPD at different superficial gas velocities are shown for two tank sizes, and computational results are compared with experimental ones. As expected, simulated cases were characterized by a decrease in RPD with the gas superficial velocity. For both tank diameters, the mean error was around 14%, while the maximum error was under 25%. Moreover, the maximum error was obtained at a lower gas flow rate; interestingly, the relative error decreased with the gas fraction. The average error was judged nevertheless acceptable, in the light of the computational convenience by using a periodic approach.

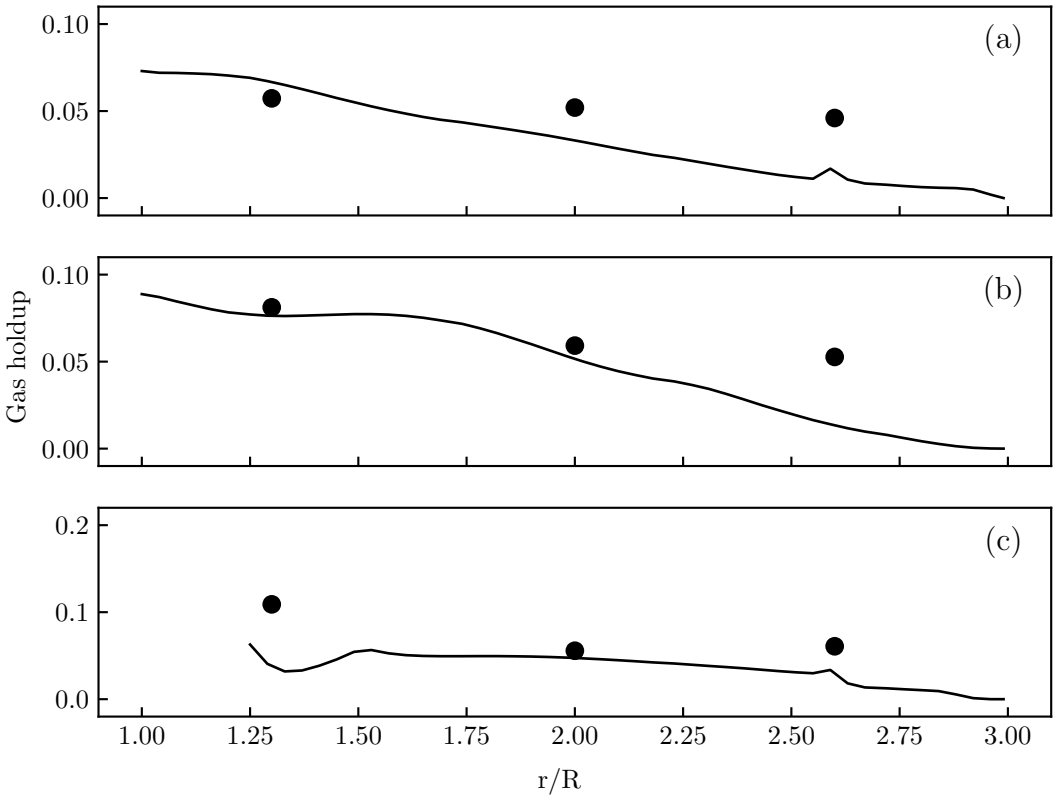

Figure 7: CFD and experimental gas fraction in water at $N = 8.3\,\mathrm{s}^{-1}$ and $U_g = 8\,\mathrm{mm\,s}^{-1}$; data were taken in T_{60} at different heights: impeller height (a), $200\,\mathrm{mm}$ (b) and $350\,\mathrm{mm}$ above the impeller disk (c). Symbols: CFD (—), experimental (●).

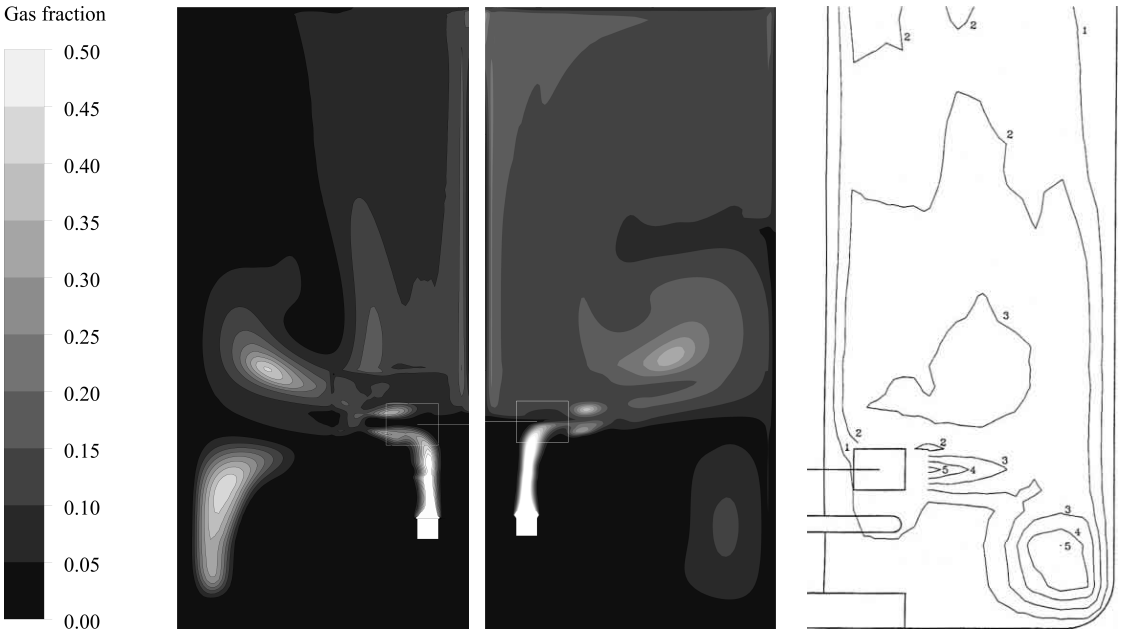

Figure 8: Contours of gas fraction in water in the VC regime based on CFD simulation for T_{30} (a) and for 1B (b), and measured by Bombač et al. (1997) (c). In order to compare the different cases, the same Froude and Flow numbers were considered.

Explanations for the discrepancy at lower gas flow rates can be found by investigating the gas accumulation behind the impeller blade. In figures 10a and 10b, the shape of the aerated cavity is highlighted; it can be seen that both simulations were characterized by the formation of a clinging cavity. At the considered operating conditions, however, gas should form a vortex cavity (Paul et al., 2004).

Liquid velocity and mixing time. In figure 11, the profile of the liquid radial velocity along the impeller blade is displayed; the liquid velocity for the single phase flow was reported as a reference.

Simulated data at different gas flow rates were compared to new measurements made with the Pavlov tube. This measuring technique is detailed in Forret et al. (2003) and it was adapted in this study to measure the liquid velocity inside the tank T_{60}. The Pavlov tube makes it possible to measure the liquid velocity at high gas flow rates; however, its accuracy decreases at higher absolute liquid velocity. For this reason, only the velocity profiles close to the impeller could be obtained. At $U_g = 1\,\mathrm{mm\,s^{-1}}$, the CFD profile followed qualitatively the experimental parabolic trend, with good agreement with measurements far from the center of the disk. Here, the numerical V/V_{tip} was approximately 20% lower than the experimental value. An increase in gas flow rate caused a further decrease in the velocity at $z = 0$; the relative error with the measured value was again $\approx 20\%$.

Concerning the mixing time, CFD simulations are compared with a new set of experimental data. Mixing times were measured in the tank T_{30} at $U_g = 8\,\mathrm{mm\,s^{-1}}$ and various values of impeller

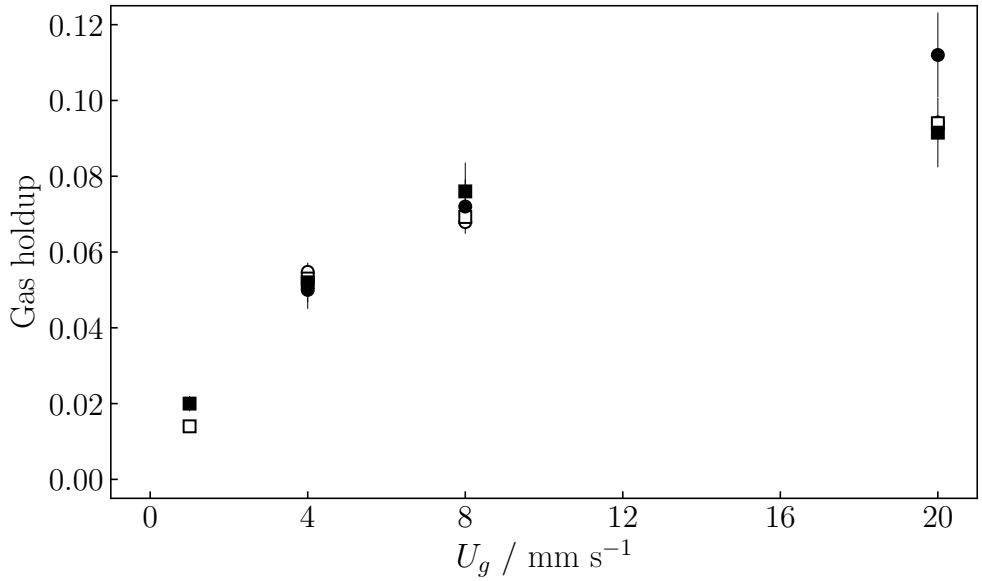

(a)

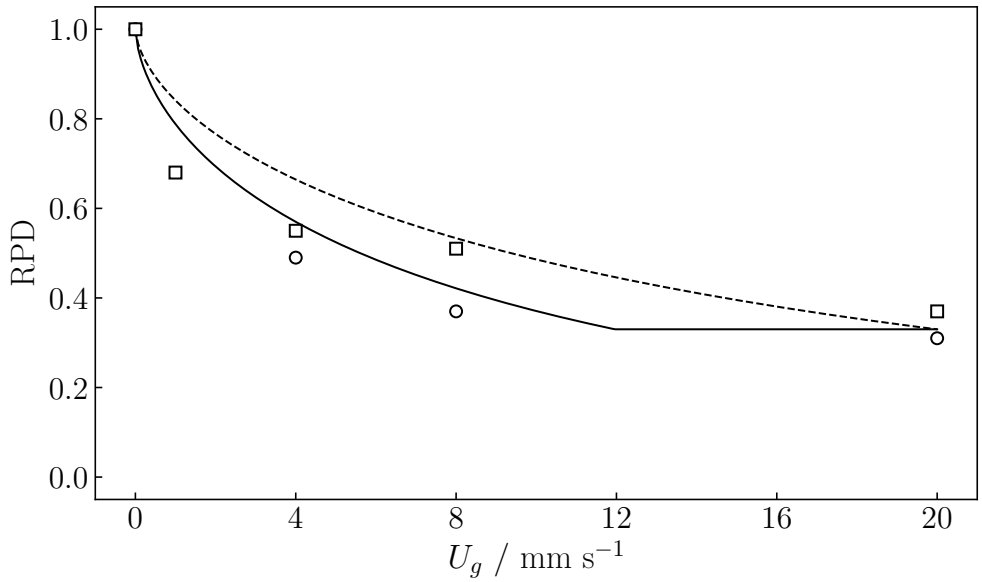

(b)

Figure 9: Numerical and measured gas holdup (a) and RPD (b) against superficial gas velocity for two tanks with different diameters. T_{30}: CFD (○), experimental (●), Eq. (14) (—); T_{60}: CFD (□), experimental (■), Eq. (14) (----).

speed. The measuring method is described in Gabelle (2012). The mixing time was computed by CFD by the mean of the transport of a passive scalar. The dispersion of passive scalars in bubbly flows is a complex field of research. Some authors have suggested to include the effect of Bubble Induced Turbulence (BIT) via k and ε source terms, indirectly impacting the turbulent viscosity

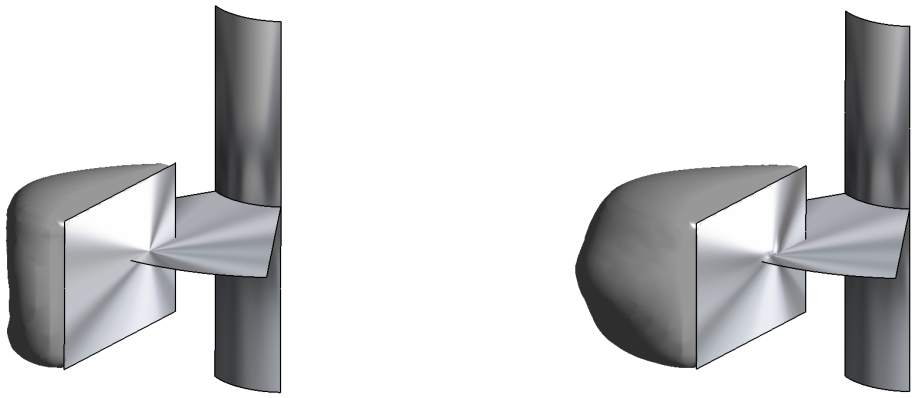

(a) (b)

Figure 10: Isosurface of gas fraction ($\alpha_g = 0.5$) at $U_g = 1\,\mathrm{mm\,s^{-1}}$ (a) and $U_g = 4\,\mathrm{mm\,s^{-1}}$ (b).

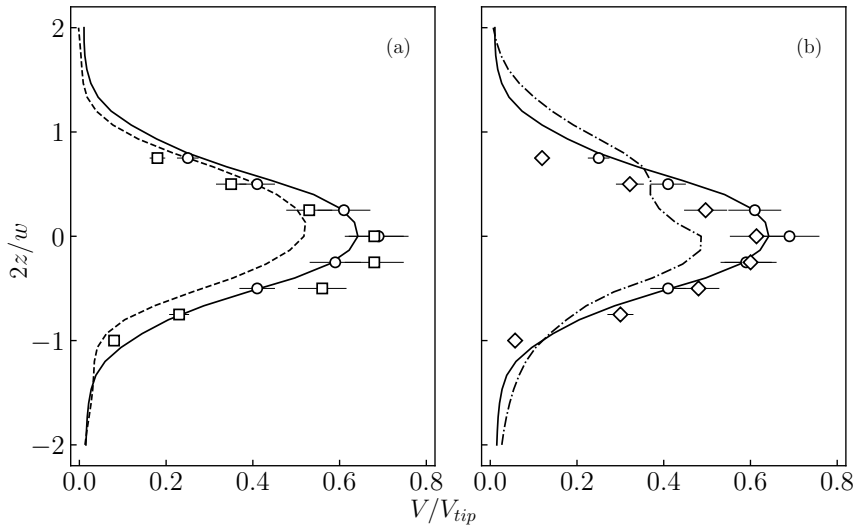

Figure 11: Profile of radial velocity along the blade height (w) at the impeller tip in air-water system, for $N = 5.8\,\mathrm{s^{-1}}$ and $U_g = 1\,\mathrm{mm\,s^{-1}}$ (a) and $U_g = 4\,\mathrm{mm\,s^{-1}}$ (b). Experimental data: $U_g = 0$ (○), $U_g = 1\,\mathrm{mm\,s^{-1}}$ (□), $U_g = 4\,\mathrm{mm\,s^{-1}}$ (◇); simulation: $U_g = 0$ (——), $U_g = 1\,\mathrm{mm\,s^{-1}}$ (- - - -), $U_g = 4\,\mathrm{mm\,s^{-1}}$ (-·-·-).

and thus the turbulent dispersion (Yao and Morel, 2004). Others suggested the use of an additional contribution to the dispersion, directly linked to presence of bubbles in the media (Alméras et al., 2015).

An ulterior method, more pragmatic, to increase dispersion of scalars consists in reducing the turbulent Schmidt number (Montante et al., 2005; Gualtieri et al., 2017). In the present study, first attempts with $Sc_t = 0.7$ and involving the BIT dispersion model of Alméras et al. (2016) led to strong overestimation of the mixing times. This result deviates from previous studies focused on bubbly flows (Alméras et al., 2016) and suggests an underestimation of the global turbulent

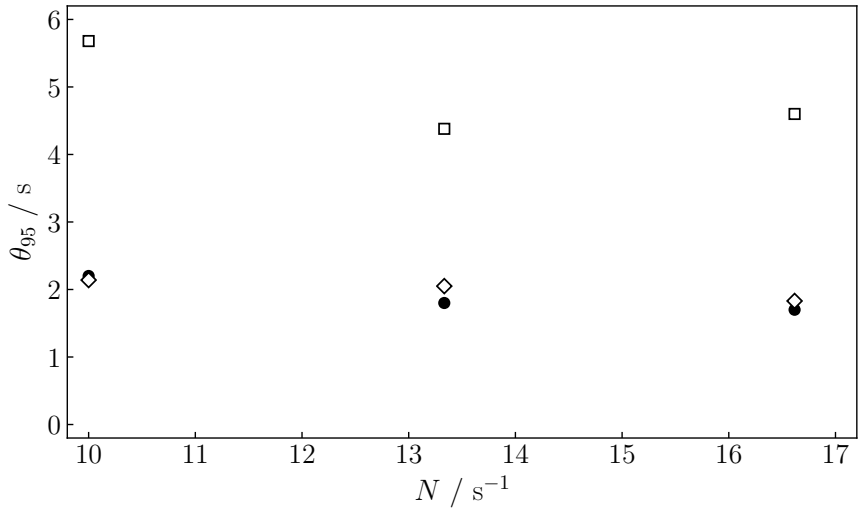

Figure 12: Effect of turbulent Schmidt number on computed mixing time. Comparison with experimental data in T_{30}. Symbols: experimental (●), $Sc_t = 0.7$ (□), $Sc_t = 0.1$ (◇).

dispersion. Finally, the best accuracy was found with the value $Sc_t = 0.1$, as it can be seen in figure 12. However, from the here presented numerical results, it seems clear that this contribution should be included in the model to improve its performance. This was not the main goal of this study, so the approach based on tweaking of turbulent Schmidt number was retained. Although this strategy is commonly adopted in the scientific community, it clearly affects the predictive potential of the model.

3.1.3. Viscosity impact

Global holdup and gassed power draw. In modeling of multiphase flows with complex rheology, the universal drag laws did not give physical results and air-xanthan simulations were characterized by accumulation of gas in regions of the vessel where the liquid had a very low velocity. Therefore, in the case of viscous non-Newtonian fluids, the drag model proposed by Scargiali et al. (2007) was preferred, because it only depends on the bubble terminal velocity and the viscosity of the liquid is not explicitly taken into account.

Figure 13a describes the mean holdup in xanthan gum solutions. In the case of XG 0.25%, an increase in gas holdup with the superficial gas velocity followed experimental findings. Except at the lowest gas flow rate, relative errors were below 3%. However, cases at higher concentration of xanthan gum were characterized by a greater mean error (25%). At $U_g = 40\,\mathrm{mm\,s^{-1}}$, the case for xanthan gum 0.50% did not reach convergence. In fact, the monitored quantities oscillated within $\pm 10\%$ respect to their final value.

The power loss due to aeration is reported for XG in figure 13b. No differences were noticed between the two concentrations. With an average error of 12%, it was found that the RPD was well predicted also in shear-thinning liquids.

Mixing time. Tweaking of the turbulent Schmidt number was necessary also for multiphase simulations of the model fluids. In figure 14, numerical θ_{95} values are presented and the effect of Sc_t

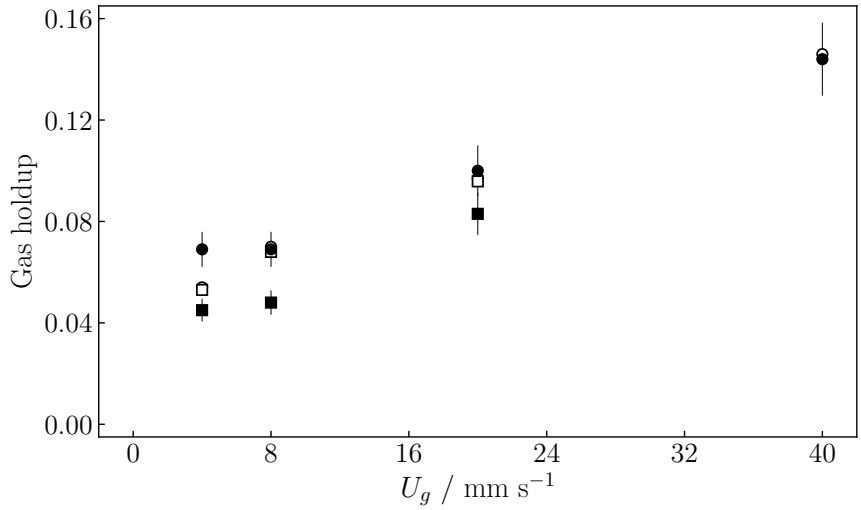

(a)

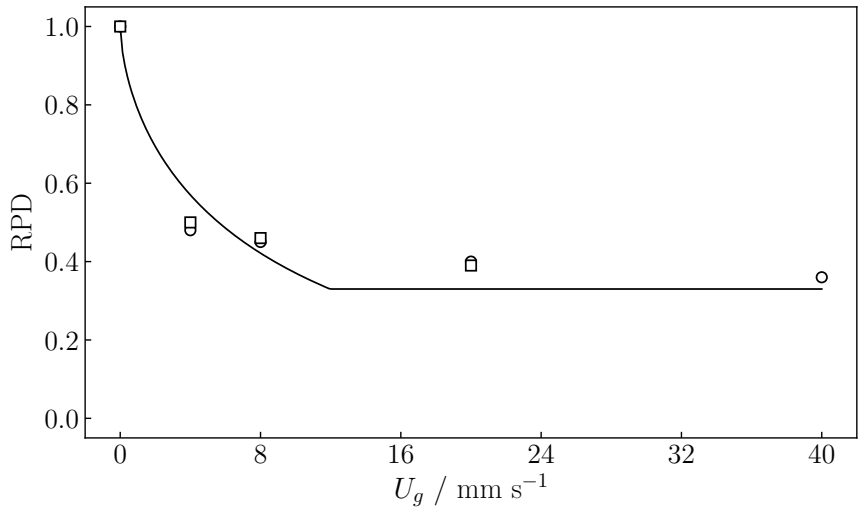

(b)

Figure 13: Numerical and measured gas holdup (a) and RPD (b) in XG against superficial gas velocity. XG 0.25%: CFD (○), experimental (●); XG 0.50%: CFD (□), experimental (■), Eq. (14) (—).

is shown. A typical value of the turbulent Schmidt number (0.7) led to overestimation of mixing time. To decrease the relative error up to 15%, a low value of the Schmidt number had to be used. Tuning of the Sc_t with experimental data did not address the problem, represented by the weakness of the multiphase turbulence model. Although useful, this approach only bypassed the poor representation of turbulent mixing in aerated media. However, by doing so, one can improve the performance of the model, which applicability can be extended to cases with similar operating conditions (Gualtieri et al., 2017).

Even though the local gas fraction was not precisely represented at the smaller scales, global

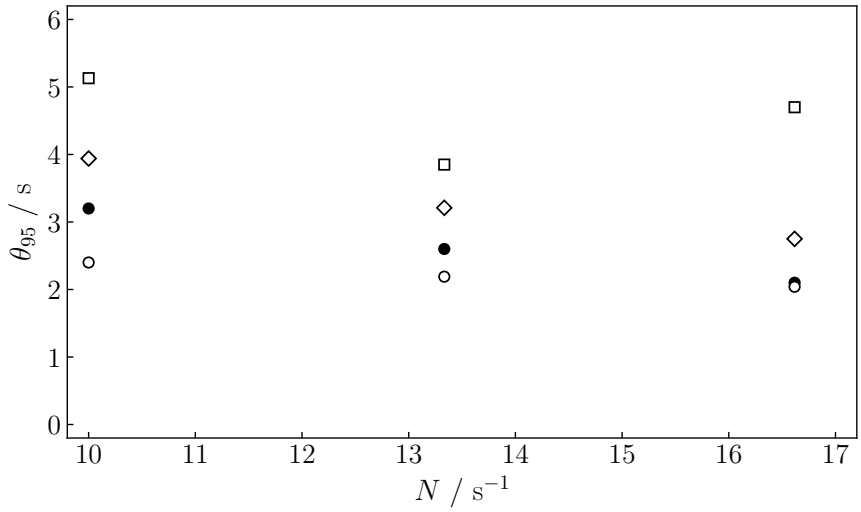

Figure 14: Mixing time in XG 0.25% at different Schmidt numbers. Experimental (●), $Sc_t = 0.7$ (□), $Sc_t = 0.2$ (◇), $Sc_t = 0.1$ (○).

characteristics such as the RPD, the global gas holdup, and the volumetric mass transfer coefficient were satisfactorily predicted; therefore, the adopted approach can be used to evaluate the scale-up of aerobic fermentations.

3.2. Application of the CFD model

3.2.1. Volumetric mass transfer prediction

The numerical volumetric mass transfer coefficient was compared to experimental values previously obtained (Cappello et al., 2020); this comparison is shown in figure 15.

In the case of water, the computed mass transfer coefficient was underpredicted in almost all cases. Nevertheless, the average discard with the experimental values was about 25%. This difference may be partially explained by an underestimation of the average interfacial area, which is linked to the discrepancy in terms of local gas fraction discussed previously (figure 8). Moreover, it was difficult to correlate the error in terms of operating conditions, as the discrepancy did not increase neither with the gas flow rate, nor with the impeller rotation speed. In the case of xanthan gum solutions, the average error was slightly higher than before (28%).

3.2.2. Fermentation of Trichoderma reesei: scale-up effect

Case at q^I_{feed}. In figure 16, the substrate concentration and q^*_P contours are displayed for both single-impeller configurations. For the small tank, the circulation time was very short compared to the characteristic time of substrate consumption, and a homogeneous concentration of sugar was obtained in the liquid (figure 16a). In fact, except for a small area close to the injection point, C_S varied between 0.0001–$0.002\,\mathrm{g\,L^{-1}}$, with an average concentration of about $0.001\,\mathrm{g\,L^{-1}}$ in the rest of the tank. On the other hand, a clear gradient of C_S was obtained for the case 1B (figure 16b); the characteristic time to consume the substrate was shorter than the circulation time, so the reactant accumulated in the region close to the feed point, where it reached a concentration in the order of

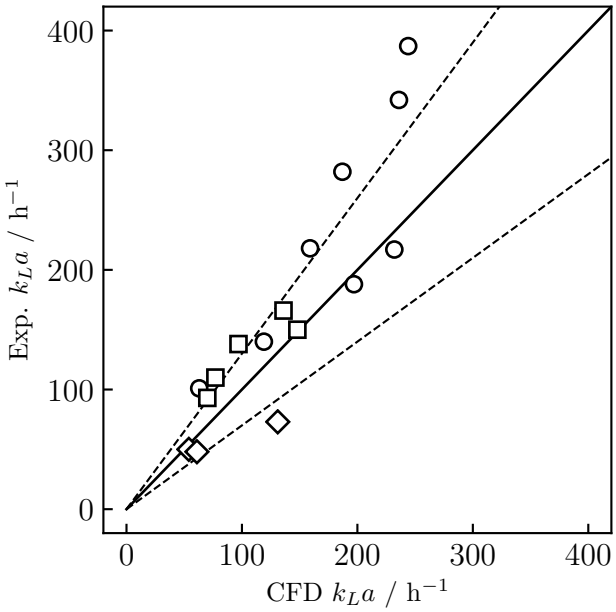

Figure 15: Average volumetric mass transfer coefficient from simulations and experiments. Data are for water (○), xanthan gum 0.25% (□), and xanthan gum 0.50% (◇); the dashed lines represent an error ±30%.

$1 \cdot 10^{-2}\,\mathrm{g\,L^{-1}}$. Moreover, the average concentration was equal to $0.002\,\mathrm{g\,L^{-1}}$; computation of the coefficient of variation for both the tanks gave 0.3 for the small one, whereas CV = 3 for the tank of $98\,\mathrm{m^3}$. The dissolved oxygen was homogeneous in both cases, and its average concentration was $5.97 \cdot 10^{-3}$ and $5.90 \cdot 10^{-3}\,\mathrm{g\,L^{-1}}$ for 1S and 1B, respectively.

The presence of a substrate gradient had consequences on the protein production rate. As it can be seen in figures 16c and 16d, the minimum and the maximum value of q_P^* was different between the two scales. Furthermore, because of the accumulation of substrate, in the tank 1B a broader volume was characterized by a higher q_P^*; in the same configuration, the specific productivity below the impeller dropped to 20% of the maximum value.

In figure 17, the volume distribution of C_S and q_P^* at the low substrate feed rate is shown. In comparison to the small reactor, the 1B configuration was characterized by a broader distribution, with a certain fraction of cells in which the normalized production rate was very high (≈ 0.7). This high-productivity area was however limited to the volume close to the injection point, where the highest substrate concentration was reached. The specific production rate was the same in both cases (table 7); at this substrate feed rate, the growth rate was practically null, so the substrate would be consumed to only produce proteins.

Hydrodynamics in multi-impeller reactors is more complex, due to the superimposed flows originated by every turbine. In the case of radial-flow turbines, axial mixing through the radial discharge is hindered, causing the formation of compartments. Although the mixing in each compartment can be fast, the global homogenization is slow. Figure 18a shows the effect of said increase in mixing time for the configuration 4R. Substrate heterogeneities caused a wide distri-

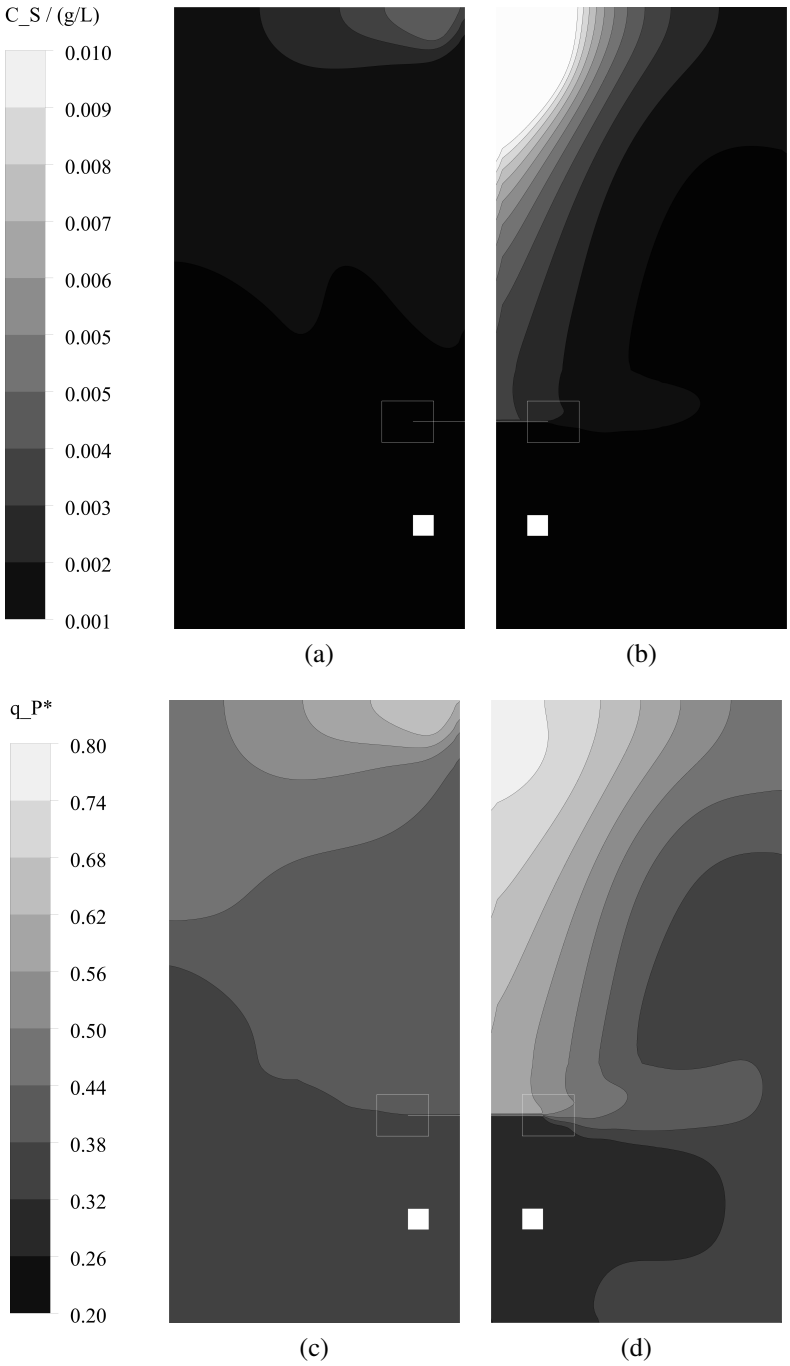

Figure 16: Substrate concentration and production rate distributions at low substrate feed rate q^I_{feed} for the cases 1S (a,c) and 1B (b,d).

bution of the production rate, as reported in figure 17. The average specific production rate was practically equal in all three cases, because the same feed rate was considered and, due to the low C_S, no microbial growth was promoted. However, in the case 4R, a wide portion of the reactor

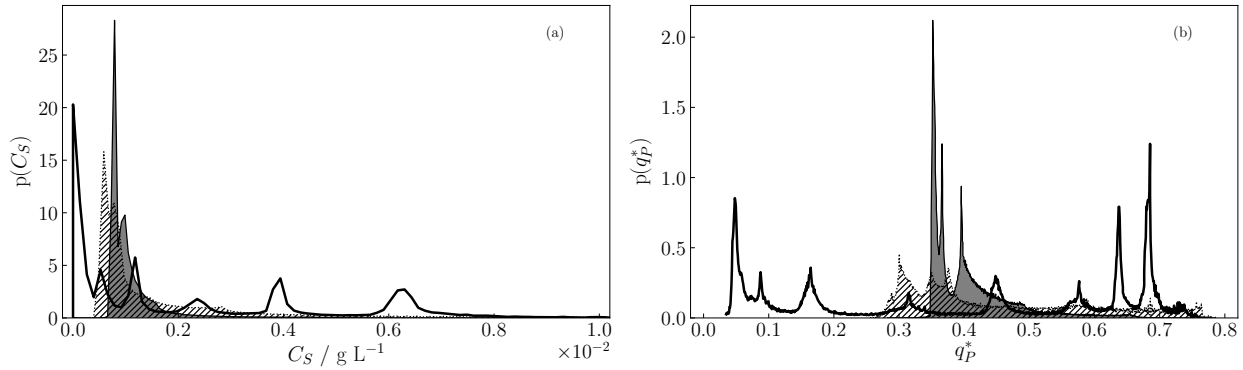

Figure 17: Volumetric distribution of substrate concentration (a) and normalized production rate (b) at q_{feed}^{I}; the y-values are normalized so that the area under each curve is equal to one. The area in gray describes data for 1S, whereas data for 1B and 4R are represented by the hatched and empty areas, respectively.

was characterized by $q_P^* < 0.2$; quantification of these zones that are poor in nutrient is important to estimate the exposure time of microbial cells in drastic conditions.

Although at this nutrient feed rate the average q_P^* was the same at every scale, one should also consider the dynamics of the process. In fact, in this analysis any cell adaptation dynamics was not considered, saying that microorganisms would instantaneously react solely based on the properties of the liquid phase (Morchain et al., 2014; Bach, 2018). Additionally, microorganisms could be permanently affected by exposure to poor zones, decreasing the protein yield. Therefore, in the case of the real process, the presence of a zone in the tank in which the productivity is high, might not entirely counterbalance those regions at low q_P due to the heterogeneous distribution of the nutrients.

Case at q_{feed}^{II}. At q_{feed}^{II} the average substrate concentration was higher than $0.2\,\mathrm{g\,L^{-1}}$ for every geometry. In this condition, growth of the microorganisms may become competitive with the production of enzyme, causing a decrease in the protein yield. Referring to table 5, the reaction time at this q_{feed} was an order of magnitude higher than the circulation time computed for the configuration 4R; therefore, even at this scale, homogenization of the nutrient species was foreseen. In the four-impeller reactor, the substrate concentration varied between 0.47–$0.54\,\mathrm{g\,L^{-1}}$ (figure 18b) with a coefficient of variation of 0.02.

The average final concentrations of substrate, oxygen, and the average production and growth rates are shown in figure 19. Numerical values were compared to average results obtained by solving Eq. (8) and Eq. (9) for the ideal-mixing case and for two different k_La values; one solution of the equations was obtained for the same k_La that characterized the simulations, while for the other k_La a value of $200\,\mathrm{h^{-1}}$ was used. The latter was chosen high enough to guarantee a high dissolved oxygen concentration. The comparison with these two ideal-mixing cases allowed one to dissociate the effects of the non-ideal mixing and of oxygen limitation. Simulation of the case 1S led to results very similar to the ideal-mixing case, as expected from the analysis of the Damköhler number. However, the average substrate concentration in the configurations 1B and 4R was higher (figure 19). This increase generated a greater oxygen demand in the bigger reactors, leading to

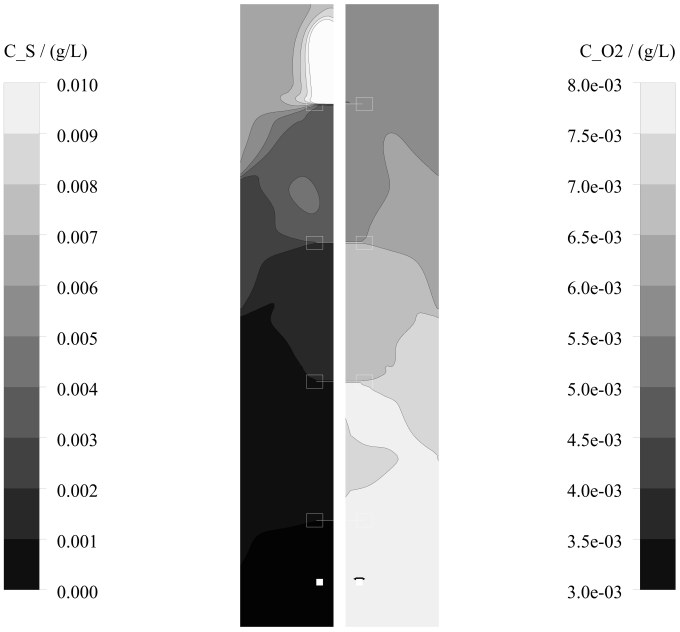

(a)

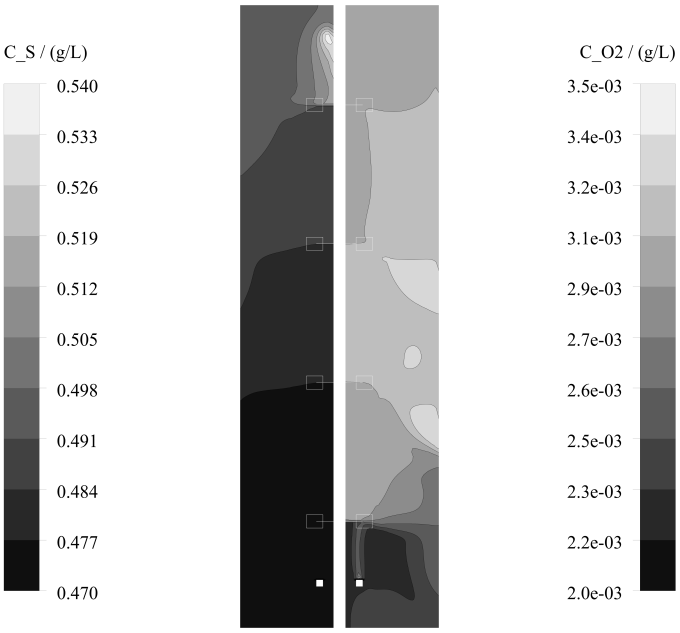

(b)

Figure 18: Species concentrations for the 4R geometry at q^{I}_{feed} (a) and q^{II}_{feed} (b).

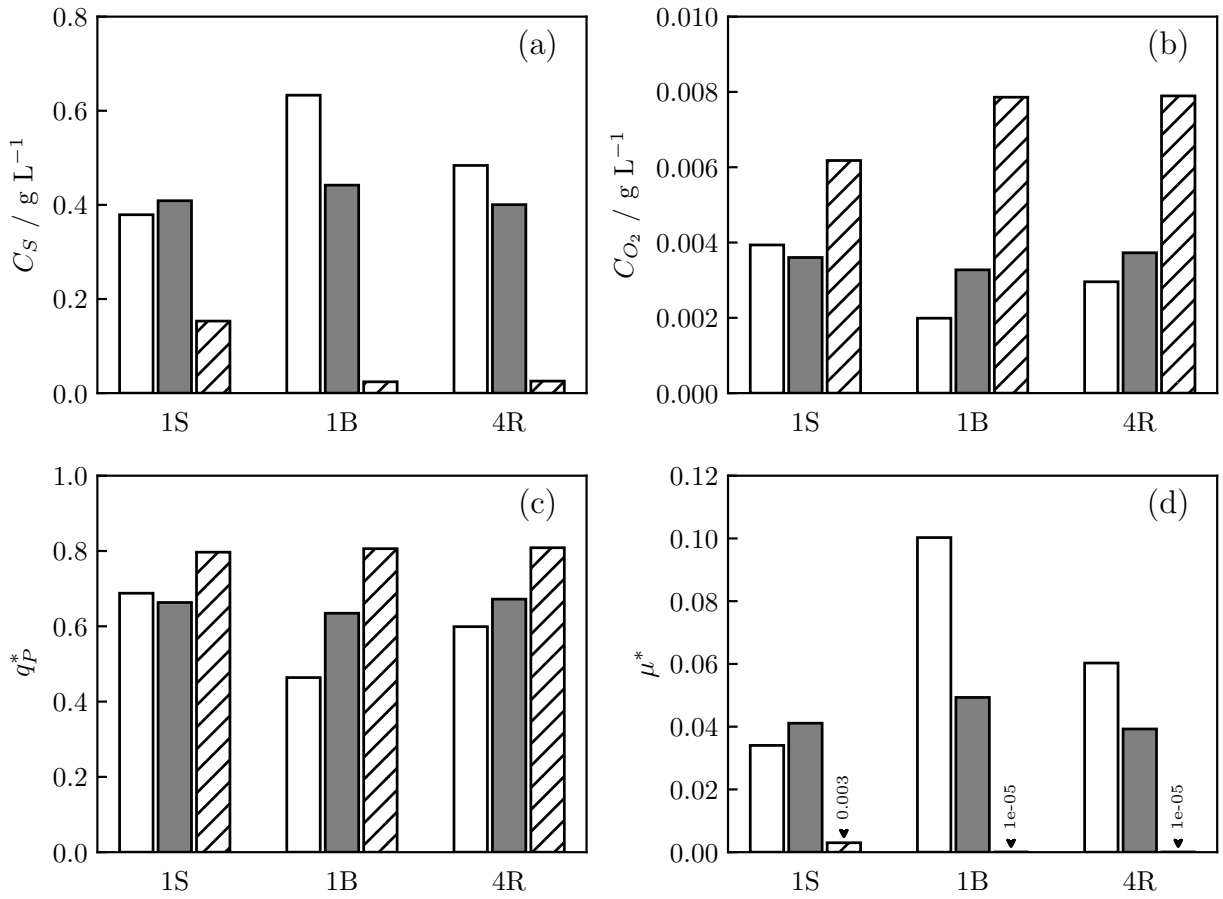

Figure 19: Nutrients concentration (a,b) and normalized production (c) and growth (d) rates for the case q^{II}_{feed}. CFD and perfect-mixing values are reported in white and gray, respectively. The hatched bars represent estimated values at $k_La = 200\,\mathrm{h}^{-1}$.

a residual oxygen concentration lower than the one of the perfectly-mixed reactor (figure 19b). The deviation from the ideal reactor condition caused a decrease in the production yield, as it can be seen in figure 19c,d. Going from 1S to 1B, the specific production rate went down of about 30%. In this case, due to the accumulation of substrate in the fermenter, the cell growth became much more competitive, causing a productivity loss; compared to the configuration 1S, the specific growth rate in 1B increased of almost 200%. A similar decrease in the reactor performance was found for the configuration 4R as well, with an increase in substrate concentration of 24%. The different content in nutrients caused a 13% loss of the specific production rate, and an almost two-fold augmentation of growth rate.

To facilitate the comparison between the different configurations and operating conditions, data presented above are collected in table 7. As expected, by increasing the feed rate, the substrate concentration in any reactor became higher. Moreover, hydrodynamics impacted the substrate distribution. Due to the high circulation time and relatively low reaction time, Da was greater than one for 4R at q^I_{feed}, thus substrate gradients were found; this case study was characterized by

Table 7: Average concentrations and kinetic rates for the CFD simulations discussed in section 3.2.2. The Damköhler number and the Coefficient of Variation are reported as well.

Case	Da / s	$CV\,(C_S)$	$\langle C_S \rangle$ / g L^{-1}	$\langle C_{O_2} \rangle$ / g L^{-1}	$\langle q_P^* \rangle$	$\langle \mu^* \rangle$
q_{feed}^{I}						
1S	$9.61 \cdot 10^{-2}$	60%	$1.09 \cdot 10^{-3}$	$5.97 \cdot 10^{-3}$	$4.04 \cdot 10^{-1}$	$2.00 \cdot 10^{-9}$
1B	$5.29 \cdot 10^{-1}$	340%	$1.55 \cdot 10^{-3}$	$5.90 \cdot 10^{-3}$	$4.08 \cdot 10^{-1}$	$1.63 \cdot 10^{-7}$
4R	2.69	120%	$2.66 \cdot 10^{-3}$	$6.73 \cdot 10^{-3}$	$4.09 \cdot 10^{-1}$	$8.83 \cdot 10^{-8}$
q_{feed}^{II}						
1S	$4.85 \cdot 10^{-4}$	0.4%	$3.79 \cdot 10^{-1}$	$3.94 \cdot 10^{-3}$	$6.88 \cdot 10^{-1}$	$3.40 \cdot 10^{-2}$
1B	$2.37 \cdot 10^{-3}$	1.7%	$6.33 \cdot 10^{-1}$	$1.99 \cdot 10^{-3}$	$4.64 \cdot 10^{-1}$	$1.00 \cdot 10^{-1}$
4R	$1.31 \cdot 10^{-2}$	2.0%	$4.84 \cdot 10^{-1}$	$2.96 \cdot 10^{-3}$	$5.99 \cdot 10^{-1}$	$6.03 \cdot 10^{-2}$

a higher $\langle C_S \rangle$ compared to the simpler 1S and 1B configurations.

Scale-up studies reported at two different substrate fed rates have pointed out some important behaviors. At low substrate feed rate, the scale–up generates substrate gradients, but related effect on fermentation yield stands negligible. The enzyme production rate q_P^* is low (about 50% from $q_{P_{max}}$) but the scale-up can be qualified as "safe", as the substrate is totally converted to proteins. On the other hand, q_P^* increased at higher feed rate while becoming sensitive to scale-up. At this condition, conversion of the substrate onto protein was also affected by the reactor size, even though the substrate concentration was homogeneous in all the configurations (i.e. Da was very small). Additionally, the oxygen transfer started to limit the fermentation yield. In such conditions, scale-up appears riskier as associated performances are more difficult to predict and may lead to severe loss of both protein productivity and substrate-to-protein yield.

4. Conclusions

An Eulerian multiphase approach was used to simulate aerobic fermentation. Firstly, the numerical model was validated against experimental data previously obtained in viscous non-Newtonian fluids. The steady Multiple Reference Frame approach, together with periodic boundaries conditions, proved to be a good compromise between accuracy and computational cost. Moreover, the use of the drag force as the solely interphase term led to an acceptable estimation of the characteristic global quantities. Particularly, the universal drag laws were used in air-water simulations, for which the gas holdup and the Relative Power Demand were predicted with an error of 10% and 14%, respectively. Although the global gas content was well computed, the local gas fraction did not fully agree with experimental findings; simulations were characterized by an excessive accumulation of gas in the recirculation loops, above and below the impeller. The implementation of lift force and turbulent dispersion force did not improve the predictivity of the CFD model. However, a better distribution of the gas phase was computed at larger scale.

A different drag coefficient model was used in the case of non-Newtonian cases. At the operating conditions considered in this study, the model of Scargiali et al. (2007) gave the best results, avoiding non-physical formation of air in the liquid. Furthermore, the characterization of complex liquids required the definition of the shear rate. For the computation of local shear rate, a model based on Kolmogorov's turbulence theory was proposed in this study (Pérez et al., 2006). With these choices, the global gas holdup, the RPD, and the mixing time were satisfactorily predicted also in aerated non-Newtonian simulations.

For the estimation of the mass transfer coefficient, the k_L correlation previously proposed (Cappello et al., 2020) was implemented in the CFD model. The average k_La was predicted with a relative error of 25%.

Finally, metabolic kinetics of *Trichoderma reesei* was coupled to hydrodynamics and mass transfer. The effect of scale-up and tank geometry on fermentation yield was assessed. At a low substrate feed rate, the substrate concentration was relatively low, and the production regime was maintained regardless of the tank size. At this condition, the bigger reactors were characterized by the presence of substrate and production rate gradients. For a doubled feed rate, the reaction timescale for each configuration became much larger than the circulation time. Therefore, the nutrients concentration was homogeneously distributed in the fermenter. At the same time, due to the higher substrate content, accumulation of C_S was obtained, which caused an increase in the oxygen demand, lowering the residual oxygen concentration. As a consequence, the bigger tanks operated in oxygen-limited conditions, and the fermenter underwent a decrease in efficiency.

The numerical approach used in this study was proven to be capable to model industrial aerobic fermenters. Although the multiphase model could satisfactorily predict the average behaviors, there is room for improvements of CFD models (interphase forces, turbulent dispersion) and reaction kinetics under dynamic conditions should also be add to enhance the predictivity of the numerical model.

Nomenclature

B	Baffle width, m
C_D	Drag coefficient
C_P	Protein concentration, $\mathrm{g\,L^{-1}}$
C_S	Substrate concentration, $\mathrm{g\,L^{-1}}$
C_X	Biomass concentration, $\mathrm{g\,L^{-1}}$
C_{O_2}	Dissolved oxygen concentration, $\mathrm{g\,L^{-1}}$
$C^*_{O_2}$	Oxygen solubility in water, $\mathrm{g\,L^{-1}}$
D	Impeller diameter, m
d_{32}	Sauter mean bubble diameter, mm
Da	Damköhler number
Fl_g	Gas flow number $= Q_g\,(ND^3)^{-1}$
Fr	Impeller Froude number $= DN^2g^{-1}$
g	Gravitational acceleration, $\mathrm{m\,s^{-2}}$
H	Liquid height, m
h_D	Impeller clearance, m
h_S	Sparger clearance, m
K	Consistency index, $\mathrm{Pa\,s^n}$
k_La	Volumetric mass transfer coefficient, s
N	Impeller rotation speed, $\mathrm{s^{-1}}$
n	Flow index
N_P	Impeller power number
P_0	Power input without aeration, W
P_g	Gassed power draw, W
Q_g	Gas flow rate, $\mathrm{m^3\,s^{-1}}$

q_O Oxygen uptake, $\mathrm{g_O\,g_X^{-1}\,h^{-1}}$

q_P Specific protein production rate, $\mathrm{g_P\,g_X^{-1}\,h^{-1}}$

q_P^* Normalized protein production rate

q_S Substrate consumption rate, $\mathrm{g_S\,g_X^{-1}\,h^{-1}}$

q_{feed} Substrate feed rate, $\mathrm{g_S\,g_X^{-1}\,h^{-1}}$

Sc_t Turbulent Schmidt number

T Tank diameter, m

U_g Superficial gas velocity, $\mathrm{mm\,s^{-1}}$

U_t Bubble terminal velocity, $\mathrm{m\,s^{-1}}$

V Radial liquid velocity, $\mathrm{m\,s^{-1}}$

V_l Reactor liquid volume, $\mathrm{m^3}$

V_{tip} Impeller velocity at the blade, $\mathrm{m\,s^{-1}}$

w Impeller height, m

z Axial coordinate, m

Greek symbols

θ_S Reaction time scale, s

α_g Global gas holdup

$\dot{\gamma}$ Shear rate, $\mathrm{s^{-1}}$

ε Turbulent energy dissipation rate, $\mathrm{m^2\,s^{-3}}$

θ_c Circulation flow time, s

θ_{95} Blending time at 95% of homogeneization, s

μ^* Normalized growth rate

μ_X Specific growth rate, $\mathrm{h^{-1}}$

μ_{app} Liquid apparent viscosity, $\mathrm{Pa\,s^{-1}}$

ρ_g Gas density, $\mathrm{kg\,m^{-3}}$

ρ_l Liquid density, $\mathrm{kg\,m^{-3}}$

σ Surface tension, $\mathrm{N\,m^{-1}}$

Abbreviations

CFD Computational Fluid Dynamics

CV Coefficient of variation

MRF Multiple Reference Frame

RPD Relative Power Demand

SM Sliding Mesh

XG Xanthan gum

References

Alméras, E., Plais, C., Euzenat, F., Risso, F., Roig, V., Augier, F., 2016. Scalar mixing in bubbly flows: Experimental investigation and diffusivity modelling. Chemical Engineering Science 140, 114–122.

Alméras, E., Risso, F., Roig, V., Cazin, S., Plais, C., Augier, F., 2015. Mixing by bubble-induced turbulence. Journal of Fluid Mechanics 776, 458–474.

ANSYS Fluent Theory Guide, 2019. ANSYS Inc Release 2019 R2.

Aubin, J., Fletcher, D., Xuereb, C., 2004. Modeling turbulent flow in stirred tanks with CFD: The influence of the modeling approach, turbulence model and numerical scheme. Experimental Thermal and Fluid Science 28.

Bach, C., 2018. Modelling of Gradients in Large Scale Bioreactors. Ph.D. thesis. Technical University of Denmark (DTU).

Bach, C., Yang, J., Larsson, H., Stocks, S.M., Gernaey, K.V., Albaek, M.O., Krühne, U., 2017. Evaluation of mixing and mass transfer in a stirred pilot scale bioreactor utilizing CFD. Chemical Engineering Science 171, 19–26.

Bombač, A., Žun, I., Filipič, B., Žumer, M., 1997. Gas-filled cavity structures and local void fraction distribution in aerated stirred vessel. AIChE journal 43, 2921–2931.

Cappello, V., Plais, C., Vial, C., Augier, F., 2020. Bubble size and liquid-side mass transfer coefficient measurements in aerated stirred tank reactors with non-Newtonian liquids. Chemical Engineering Science 211, 115280.

Deglon, D., Meyer, C., 2006. CFD modelling of stirred tanks: Numerical considerations. Minerals Engineering 19, 1059–1068.

Doran, P.M., 2013. Chapter 8 - mixing, in: Doran, P.M. (Ed.), Bioprocess Engineering Principles (Second Edition). second edition ed.. Academic Press, pp. 255 – 332.

Enfors, S.O., Jahic, M., Rozkov, A., Xu, B., Hecker, M., Jürgen, B., Krüger, E., Schweder, T., Hamer, G., O'beirne, D., et al., 2001. Physiological responses to mixing in large scale bioreactors. Journal of biotechnology 85, 175–185.

Forret, A., Schweitzer, J.M., Gauthier, T., Krishna, R., Schweich, D., 2003. Influence of scale on the hydrodynamics of bubble column reactors: An experimental study in columns of 0.1, 0.4 and 1 m diameters. Chemical Engineering Science 58, 719–724.

Gabelle, J.C., 2012. Analyse locale et globale de l'hydrodynamique et du transfert de matière dans des fluides à rhéologie complexe caractéristiques des milieux de fermentation. Ph.D. thesis. Toulouse, INSA.

Gabelle, J.C., Augier, F., Carvalho, A., Rousset, R., Morchain, J., 2011. Effect of tank size on k_La and mixing time in aerated stirred reactors with non-Newtonian fluids. The Canadian Journal of Chemical Engineering 89, 1139–1153.

Gabelle, J.C., Jourdier, E., Licht, R., Chaabane, F.B., Henaut, I., Morchain, J., Augier, F., 2012. Impact of rheology on the mass transfer coefficient during the growth phase of Trichoderma reesei in stirred bioreactors. Chemical Engineering Science 75, 408–417.

Gimbun, J., Rielly, C.D., Nagy, Z.K., 2009. Modelling of mass transfer in gas–liquid stirred tanks agitated by rushton turbine and cd-6 impeller: A scale-up study. Chemical Engineering Research and Design 87, 437–451.

Gradov, D.V., Laari, A., Turunen, I., Koiranen, T., 2017. Experimentally validated CFD model for gas-liquid flow in a round-bottom stirred tank equipped with rushton turbine. International Journal of Chemical Reactor Engineering 15.

Gualtieri, C., Angeloudis, A., Bombardelli, F., Jha, S., Stoesser, T., 2017. On the values for the turbulent Schmidt number in environmental flows. Fluids 2, 1–27.

Gusakov, A.V., 2011. Alternatives to Trichoderma reesei in biofuel production. Trends in biotechnology 29, 419–425.

Haringa, C., Tang, W., Deshmukh, A.T., Xia, J., Reuss, M., Heijnen, J.J., Mudde, R.F., Noorman, H.J., 2016. Euler-Lagrange computational fluid dynamics for (bio) reactor scale down: an analysis of organism lifelines. Engineering in life sciences 16, 652–663.

Haringa, C., Tang, W., Wang, G., Deshmukh, A.T., van Winden, W.A., Chu, J., van Gulik, W.M., Heijnen, J.J., Mudde, R.F., Noorman, H.J., 2018. Computational fluid dynamics simulation of an industrial P. chrysogenum fermentation with a coupled 9-pool metabolic model: Towards rational scale-down and design optimization. Chemical Engineering Science 175, 12–24.

Keating, M., 2011. Accelerating CFD solutions. ANSYS Advantage V, 48–49.

Lane, G., Schwarz, M., Evans, G.M., 2005. Numerical modelling of gas–liquid flow in stirred tanks. Chemical Engineering Science 60, 2203–2214.

Lane, G.L., 2017. Improving the accuracy of CFD predictions of turbulence in a tank stirred by a hydrofoil impeller. Chemical Engineering Science 169, 188–211.

Li, Y., Liu, C., Bai, F., Zhao, X., 2016. Overproduction of cellulase by Trichoderma reesei rut c30 through batch-feeding of synthesized low-cost sugar mixture. Bioresource technology 216, 503–510.

Liangchao, L., Ning, C., Kefeng, X., Beiping, X., 2018. A comparative CFD study on gas-liquid dispersion in a stirred tank with low and high gas loadings. International Journal of Chemical Reactor Engineering 16.

Lo, C.M., Zhang, Q., Callow, N.V., Ju, L.K., 2010. Roles of extracellular lactose hydrolysis in cellulase production by trichoderma reesei rut c30 using lactose as inducing substrate. Process Biochemistry 45, 1494–1503.

Mendelson, H.D., 1967. The prediction of bubble terminal velocities from wave theory. AIChE Journal 13, 250–253.

Montante, G., Moštěk, M., Jahoda, M., Magelli, F., 2005. CFD simulations and experimental validation of homogenisation curves and mixing time in stirred Newtonian and pseudoplastic liquids. Chemical Engineering Science 60, 2427–2437.

Morchain, J., Gabelle, J.C., Cockx, A., 2014. A coupled population balance model and CFD approach for the simulation of mixing issues in lab-scale and industrial bioreactors. AIChE Journal 60, 27–40.

Oosterhuis, N.M.G., Kossen, N.W.F., Olivier, A.P.C., Schenk, E.S., 1985. Scale-down and optimization studies of the gluconic acid fermentation by Gluconobacter oxydans. Biotechnology and Bioengineering 27, 711–720.

Paul, E.L., Atiemo-Obeng, V.A., Kresta, S.M., 2004. Handbook of industrial mixing: science and practice. John Wiley & Sons.

Petříček, R., Moucha, T., Rejl, F.J., Valenz, L., Haidl, J., Čmelíková, T., 2018. Volumetric mass transfer coefficient, power input and gas hold-up in viscous liquid in mechanically agitated fermenters. measurements and scale-up. International Journal of Heat and Mass Transfer 124, 1117–1135.

Pérez, J.A.S., Porcel, E.M.R., López, J.L.C., Sevilla, J.M.F., Chisti, Y., 2006. Shear rate in stirred tank and bubble column bioreactors. Chemical Engineering Journal 124, 1 – 5.

Scargiali, F., D'Orazio, A., Grisafi, F., Brucato, A., 2007. Modelling and simulation of gas–liquid hydrodynamics in mechanically stirred tanks. Chemical Engineering Research and Design 85, 637–646.

Shi, P., Rzehak, R., 2018. Bubbly flow in stirred tanks: Euler-Euler/RANS modeling. Chemical Engineering Science 190, 419–435.

Singh, H., Fletcher, D.F., Nijdam, J.J., 2011. An assessment of different turbulence models for predicting flow in a baffled tank stirred with a rushton turbine. Chemical Engineering Science 66, 5976–5988.

Yao, W., Morel, C., 2004. Volumetric interfacial area prediction in upward bubbly two-phase flow. International Journal of Heat and Mass Transfer 47, 307–328.